

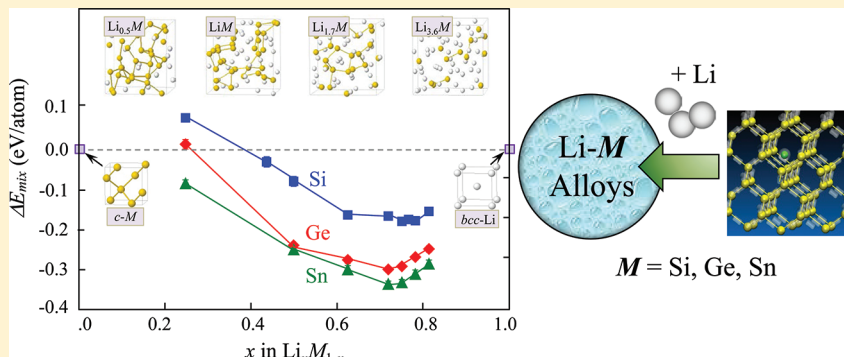
A Comparative First-Principles Study of the Structure, Energetics, and Properties of Li–M (M = Si, Ge, Sn) Alloys

Chia-Yun Chou,[†] Hyunwoo Kim,[‡] and Gyeong S. Hwang^{*,†,‡}

[†]Materials Science and Engineering Program, University of Texas at Austin, Austin, Texas 78712, United States

[‡]Department of Chemical Engineering, University of Texas at Austin, Austin, Texas 78712, United States

ABSTRACT:



On the basis of density functional theory calculations, we first present a comparative study on the behavior of Li atoms in M (M = Si, Ge, and Sn) and evaluate how Li incorporation affects the electronic structure and bonding nature of the host lattices. We then discuss the energetics, structural evolution, and variations in electronic and mechanical properties of crystalline and amorphous Li–M alloys. Our calculations show that Li insertion is the least favorable in Si and the most favorable in Sn owing to its large effective interstitial space and softer matrix. Upon Li incorporation, the bonding strength of the host network is weakened, attributed to the transferred charge from Li. Li interstitials can migrate easily in all three host materials with a moderate migration barrier in Si and small barriers in Ge and Sn. Because of the cationic nature of Li, Li atoms tend to remain isolated and well dispersed in M; also induced by this cationic nature is the charge redistribution toward Li, leading to the strong screening/shielding effect in Si, in which the excess charges are highly localized, and a relatively weaker effect in Sn. According to our mixing enthalpy calculations, alloying between Li and M is energetically favorable with Li–Sn alloys being the most stable, followed by Li–Ge and Li–Si alloys. On the basis of structural, electronic, and mechanical property analyses, we also demonstrate how the incorporation of Li atoms with increasing concentration leads to the disintegration of host networks and softening of the Li–M alloys, and associated with the more flexible lattices, the volume expansion at fully lithiated states are 434 (399)% (Si), 382 (353)% (Ge), and 305 (259)% (Sn) for amorphous (crystalline) Li–M alloys.

1. INTRODUCTION

The growing demands for safer lithium-ion batteries (LIBs) with higher capacity and longer durability have led to the search for next-generation electrode materials. Although the most widely used graphite anodes in LIBs have good cycling performance with a theoretical capacity of 372 mAh g⁻¹ (LiC₆), other group IV semiconductors (Si, Ge, Sn) can offer significantly higher capacities: 4200 mAh g⁻¹ for Li_{4.4}Si, 1600 mAh g⁻¹ for Li_{4.4}Ge, and 990 mAh g⁻¹ for Li_{4.4}Sn.^{1,2} In addition to the large increase in energy-storage capacity, lithium–group IV alloys (Li–M, M = Si, Ge, Sn) also have a safe thermodynamic potential, making them attractive candidates for LIB anodes. However, the practical use of Si, Ge, or Sn as an anode material is hindered by its poor cycling ability. In particular, the large volume change during the lithiation/delithiation process (up to 400% for Si, 370% for Ge, and 300% for Sn)^{3–5} can cause cracking and pulverization of the electrodes. Considerable efforts have been made to overcome these problems through structural modifications^{6–11} and alloying with active/inactive

elements.^{12–16} First-principles calculations have also been applied to investigate fundamental aspects of the lithiation behavior and structural evolution of the anode materials, yet many of which still remain unclear.

Despite the similarities shared among the group IV materials, Si has received the most attention because of its highest known capacity, whereas the analogous systems have not been studied as closely, and some of their merits as an anode material may have been overlooked in the past. For instance, the diffusivity of Li in Ge is about 400 times greater than that of Li in Si at room temperature,¹⁷ which may contribute to faster charge/discharge rates. Thus far, there has been no comprehensive comparison study on Si, Ge, and Sn as to the dynamic behavior of Li incorporation, the stability of the host lattices, and the properties of the alloys formed during lithiation.

Received: June 11, 2011

Published: September 01, 2011

In this paper, we first examine the structure, stability, Li diffusion, Li–Li interaction, and how the host lattice M (M = Si, Ge, and Sn) is affected by Li insertion using density functional theory (DFT) calculations. The group IV elements are found to adopt the diamond crystalline structure, which allows a comparative study on the nature of Li in different host materials, but the same diamond structure. Although other allotropic structures are found for Ge and Sn (β -Ge and β -Sn¹⁸), they do not serve a particular interest in this study. We then examine the structure, energetics, and mechanical and electronic properties of Li–M alloys. The structural evolution in terms of Li content is analyzed for both crystalline and amorphous phases, and the relative stabilities of the alloys are evaluated based on their mixing enthalpies. As the structure undergoes considerable changes when alloyed with Li, variations in elastic constant and bulk modulus are also analyzed to assess the relationship between the structure and the mechanical properties.

2. COMPUTATIONAL METHODS

The calculations reported herein were performed based on density functional theory (DFT) within the generalized gradient approximation (GGA-PW91)¹⁹ as implemented in the Vienna Ab-initio Simulation Package (VASP).^{20–22} The local density approximation (LDA) was also used in lattice constant and bulk modulus calculations for comparison. Spin polarization was also examined, but appears to be unimportant. The projected augmented wave (PAW) method with a plane-wave basis set was employed to describe the interaction between ion cores and valence electrons. The PAW method is, in principle, an all-electron frozen-core approach that considers exact valence wave functions. Valence configurations employed are as follows: 1s²2s¹ for Li, 3s²3p² for Si, 4s²4p² (3d¹⁰) for Ge, and 5s²5p² (4d¹⁰) for Sn. An energy cutoff of 350 eV was applied for the plane-wave expansion of the electronic eigenfunctions, except for mechanical property calculations, which employed an increased cut-off energy of 500 eV. The Si (Ge and Sn) host was modeled using a 216-atom cubic supercell. The effect of volume relaxation was also checked upon incorporating the Li interstitial, and it turns out to be unimportant as the 216-atom supercell is large enough to accommodate one or two Li atoms with no significant volume change (less than 1%). For geometry optimization and energy calculations, all atoms were fully relaxed using the conjugate gradient method until residual forces on constituent atoms become smaller than 5×10^{-2} eV/Å, and the convergence criterion was tightened to 1×10^{-3} eV/Å for mechanical property calculations. The Brillouin zone sampling for 216-atom supercells was done via a ($2 \times 2 \times 2$) k -point mesh within the Monkhorst–Pack scheme,²³ and the k -point meshes for crystalline alloys of various supercell sizes are specified in the text otherwise (Table 3). Diffusion pathways and barriers were determined using the climbing-image nudged elastic band method²⁴ with nine intermediate images for each hopping step.

The model structures of amorphous Li–M alloys (M = Si, Ge, Sn) were created using AIMD simulations based on the atomic configurations of Au–Si alloys that were previously obtained using the combined modified embedded atom method (MEAM) and AIMD simulations (see ref 25 for detailed computational methods). According to the previous study,²⁵ Au and Si atoms in the bulk Au–Si amorphous alloy are overall well-mixed with no segregation. The Au–Si interaction differs from the Li–M interaction in nature, and thus the local atomic configurations (or short-range order) of the alloys tend to be dissimilar. Nonetheless, the

Au–Si amorphous structure is likely a good starting configuration for the Li–M amorphous structures (where Li and M atoms are also well-dispersed); moreover, the high mobilities of Li and M at high temperature (>1000 K) allow facile local structure rearrangements to yield reliable Li–M configurations within a moderate annealing time. The Au atoms (in Au–Si alloys) were replaced by Li and M atoms accordingly to achieve desired composition ratios; the replacement sites were carefully chosen such that M and Li were well-dispersed. The model structures, each containing 64 Li and M atoms, were annealed at 1500 K for 2 ps with a time step of 1 fs and then rapidly quenched to 300 K at a rate of 0.6 K/fs, along with volume optimization. Here, the temperature was controlled via velocity rescaling. The annealing temperature was assured to be far above the alloy melting point (~1000 K) to accelerate the melting process and to eliminate any memory effects from the initial configuration. This approach can provide reasonable Li–M amorphous structures at a significantly reduced computational burden compared to starting with crystalline initial configurations.

3. RESULTS AND DISCUSSION

A. Single Li Atom in Crystalline Si, Ge, and Sn. *1. Structure and Formation Energy.* First, we compared the lattice spacing and rigidity of the host materials (Si, Ge, Sn). Table 1 summarizes calculated lattice constants (a) and bulk moduli (B) for diamond-structure Si, Ge, and Sn with reference values; a and B were obtained using 216-atom ($2 \times 2 \times 2$ k -points) and 8-atom ($21 \times 21 \times 21$ k -points) supercells, respectively. The bulk modulus was determined by fitting the Murnaghan equation of state²⁶ to the corresponding energy versus volume curve

$$E(V) = E_0 + \left(\frac{BV}{B'} \right) \left[\left(\frac{V_0/V}{B'-1} \right)^{B'} + 1 \right] - \frac{V_0 B}{(B'-1)}$$

where E and E_0 refer to the total energies of the supercell at volumes V and V_0 (equilibrium), respectively, B is the bulk modulus, and B' is the pressure derivative of the bulk modulus.

In our calculations, uniform tensile and compressive stresses were imposed on the systems to achieve a 10% volume variation. Our predicated values are overall in good agreement with previous theoretical and experimental results.^{27–29} The GGA (LDA) tends to overestimate (underestimate) the bond lengths due to the well-known under-binding (over-binding) problem; accordingly, the LDA values of B are consistently greater than the GGA values. For Ge and Sn, the respective 3d and 4d electrons were also included for valence electrons, but the d-electron contributions to the lattice spacing and rigidity turn out to be insignificant.

The insertion of Li at the tetrahedral interstitial site (T-site), which has been identified to be energetically the most favorable site for Li insertion,³⁰ can impose a compressive strain on the surrounding host lattice and lead to a slight outward relaxation of the neighboring atoms. To evaluate the relative ease of Li insertion and corresponding host–lattice disturbances, we calculated the neighboring atom displacements (Δ) and formation energies (E_f) for single Li insertion in the host materials considered. For the 216-atom cubic supercell employed, the displacements of the first and second nearest neighbors (NNs) are presented in Table 2. The second NNs show significantly smaller displacements than the first NNs, indicating that the mechanical strain imposed by the Li insertion drops quickly beyond the four first NNs. Among Si, Ge, and Sn lattices, Ge has the largest and Sn the smallest atomic displacements.

This result can be understood in terms of the effective interstitial space and stiffness of the host lattices. Because all three host lattices have the same crystal structure, the one with a

Table 1. Calculated Lattice Constants (*a*) and Bulk Moduli (*B*) for Si, Ge, and Sn; Values Calculated Considering d Electrons Are in Parentheses

		lattice constant, <i>a</i> (Å)	bulk modulus, <i>B</i> (GPa)
Si: 3s ² 3p ²	GGA	5.475, 5.465 ²⁷	91.3, 87.9 ²⁷
	LDA	5.402, 5.398 ²⁷	95.8, 96.2 ²⁷
	exptl	5.43 ²⁸	98.0 ²⁸
Ge: 4s ² 4p ² (3d ¹⁰ 4s ² 4p ²)	GGA	5.779 (5.758), 5.780 ²⁷	57.0 (60.4), 55.9 ²⁷
	LDA	5.650 (5.615), 5.531 ²⁷	69.5 (68.9), 73.3 ²⁷
	exptl	5.66 ²⁸	75 ²⁸
Sn: 5s ² 5p ² (4d ¹⁰ 5s ² 5p ²)	GGA	6.645 (6.647), 6.738 ²⁹	36.6 (34.5), 30.8 ²⁹
	LDA	6.510 (6.429), 6.462 ²⁹	45.6 (37.4), 43.2 ²⁹
	exptl	5.83 ²⁸	42.6 ²⁸

Table 2. Formation Energies (*E*_f) of Interstitial Li at the Tetrahedral Site in Crystalline Si, Ge, and Sn Host Lattices (216-Atom Cubic Cells) with Respect to Body-Centered Cubic Li and the Crystalline Host, Together with First- and Second-Nearest-Neighbor (NN) Displacements (Δ) Calculated with (relax V.) and without (fix V.) Relaxing the Cell Volume^a

	<i>E</i> _f (eV)	Δ , 1st NN (Å)	Δ , 2nd NN (Å)
Si	fix V.	0.403	0.086
	relax V.	0.401	0.084
Ge	fix V.	-0.274 (-0.226)	0.088 (0.080)
	relax V.	-0.285 (-0.221)	0.091 (0.079)
Sn	fix V.	-0.491 (-0.544)	0.079 (0.078)
	relax V.	-0.573 (-0.543)	0.085 (0.077)

^aValues calculated considering d electrons are in parentheses.

bigger atomic size is expected to have a larger effective space to accommodate an Li interstitial, and thus the smaller displacements of the neighboring host atoms; note that the covalent radii of Sn, Ge, and Si are 1.40, 1.22, and 1.11 Å, respectively. The same effect is also anticipated from a host lattice with a higher bulk modulus as it indicates a stiffer matrix to withstand interstitial insertion; the calculated bulk moduli for Si, Ge, and Sn are 91, 57, and 37 GPa, respectively. Sn has a relatively spacious matrix and thus yields a minimum amount of lattice displacement. Between Si and Ge, although a similar lattice structure and hence effective interstitial space are shared, the latter has a softer matrix, which allows slightly larger outward relaxation. Considering the geometrical and mechanical properties of the host lattices, our prediction of Ge with the largest and Sn the smallest outward relaxation is rational.

Also listed in Table 2 are the formation energies (*E*_f) of a Li interstitial in 216-atom c-M with respect to body-centered cubic Li (bcc-Li) and the crystalline host material (c-M, M = Si, Ge, Sn). *E*_f is calculated by

$$E_f = E_{M+Li} - E_M - E_{Li}$$

where *E*_{M+Li} is the total energy of one Li interstitial in 216-atom c-M, *E*_M is the total energy of 216-atom c-M, and *E*_{Li} is the energy of one bcc-Li atom.

Among the host lattices considered, the formation energy of interstitial Li is the lowest in Sn (-0.491 eV), higher in Ge (-0.274 eV), and is the highest in Si (0.403 eV); the more negative values indicate the relatively more favorable incorporation of Li. Energetically, the nature of Sn as a host material renders favorable Li incorporation since the associated lattice disturbance is minimal in Sn, but relatively larger in Ge and Si, as can be seen from the lattice displacement results. It is also worth mentioning that, although the effects of including d electrons and volume relaxation were considered, both turn out to be unimportant. The deviations in the formation energy due to the inclusion of d electrons are small enough to be negligible. The same can be said about the amount of lattice

Table 3. Crystallographic Parameters for Li–M (M = Si, Ge, Sn) Intermetallic Compounds (Reported in the Literature) with Experimental Values in Parentheses^a

	space group	lattice constants (Å)	#Li/#M	k-point mesh
Li	<i>I</i> m3̄ <i>m</i>	3.438 (3.513) ²⁸	16/0	α
LiSi	<i>I</i> 4 ₁ / <i>a</i>	<i>a</i> = 9.353 (9.353), <i>c</i> = 5.753 (5.743) ³⁹	8/8	β
Li ₁₂ Si ₇	<i>P</i> nma	<i>a</i> = 8.546 (8.60), <i>b</i> = 19.665 (19.755), <i>c</i> = 14.327 (14.336) ⁴⁰	96/56	γ
Li ₇ Si ₃	<i>R</i> 3̄ <i>m</i>	<i>a</i> = 4.3973 (4.435), <i>c</i> = 17.928 (18.134), γ = 120 (120) ⁴¹	40/16	β
Li ₁₃ Si ₄	<i>P</i> bam	<i>a</i> = 7.920 (7.99), <i>b</i> = 15.106 (15.21), <i>c</i> = 4.442 (4.49) ⁴¹	26/8	β
Li ₁₅ Si ₄	<i>I</i> 4̄3 <i>d</i>	10.623 (10.6857) ⁴²	60/16	β
Li ₂₂ Si ₅	<i>F</i> 23	18.651 (18.75) ⁴¹	88/20	γ
LiGe	<i>I</i> 4 ₁ / <i>a</i>	<i>a</i> = 9.846 (9.75), <i>c</i> = 5.810 (5.78) ⁴³	16/16	β
Li ₇ Ge ₂	<i>C</i> m _{mm}	<i>a</i> = 8.179 (9.24), <i>b</i> = 15.135 (13.21), <i>c</i> = 4.508 (4.63) ⁴³	28/8	β
Li ₁₅ Ge ₄	<i>I</i> 4̄3 <i>d</i>	10.698 (10.72) ⁴³	60/16	β
Li ₂₂ Ge ₅	<i>F</i> 23	18.859 (18.87) ⁴³	88/20	β
Li ₂ Sn ₅	<i>P</i> 4/ <i>mbm</i>	<i>a</i> = 10.460 (10.274), <i>c</i> = 3.080 (3.125) ⁴⁴	4/10	β
LiSn	<i>P</i> 2/ <i>m</i>	<i>a</i> = 5.197 (5.17), <i>b</i> = 7.856 (7.74), <i>c</i> = 3.121 (3.18), β = 104.5 (104.5) ⁴⁵	3/3	β
Li ₇ Sn ₃	<i>P</i> 2 ₁ / <i>m</i>	<i>a</i> = 9.44 (9.45), <i>b</i> = 8.53 (8.56), <i>c</i> = 4.71 (4.72), γ = 105.95 (105.95) ⁴⁵	14/6	β
Li ₁₃ Sn ₅	<i>P</i> 3̄ <i>m</i> 1	<i>a</i> = 4.69 (4.74), <i>c</i> = 17.04 (17.12), γ = 120 (120) ⁴⁵	13/5	β
Li ₇ Sn ₂	<i>C</i> m _{mm}	<i>a</i> = 8.578 (9.8), <i>b</i> = 15.996 (13.8), <i>c</i> = 4.714 (4.75) ⁴⁵	28/8	β
Li ₂₂ Sn ₅	<i>F</i> 23	19.660 (19.78) ⁴⁵	88/20	α

^aCalculated reference values are taken from refs 40 and 42. α = 11 × 11 × 11, β = 5 × 5 × 5, and γ = 3 × 3 × 3.

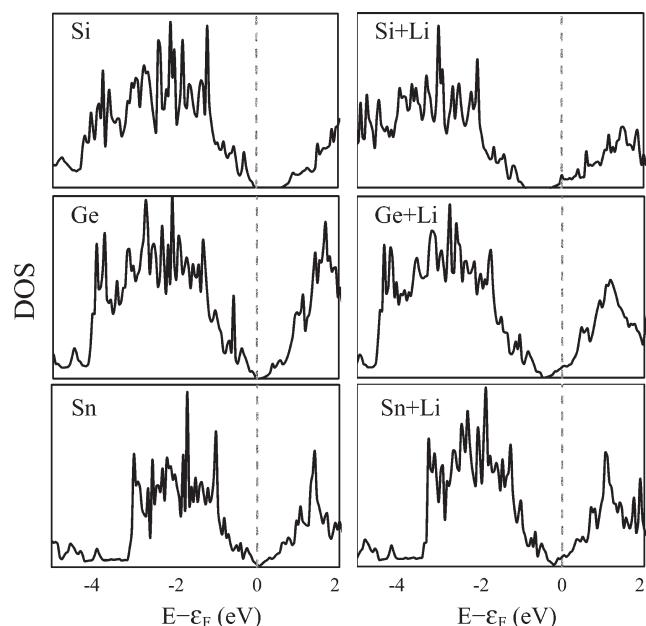


Figure 1. Electron density of states (DOS) for Si, Ge, and Sn without Li (left) and with Li (right). The vertical dotted line indicates the Fermi level (ε_F) position.

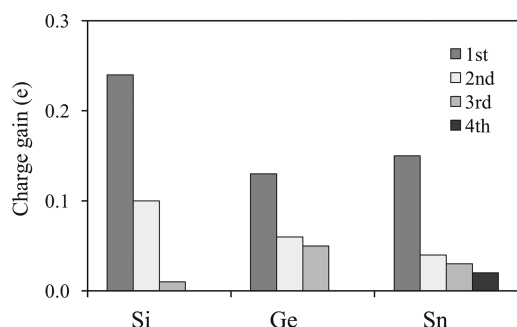


Figure 2. Charge gain (per atom) for the first, second, third, and fourth nearest neighbors in Si, Ge, and Sn. The amount of charge gain is estimated using grid-based Bader charge analysis.

displacements when considering the effect of cell volume relaxation; moreover, it has also been reported in the previous calculation³⁰ that the volume expansion associated with one Li insertion in a 216-atom supercell is very minimal (less than 1%), indicating that the cell size is sufficiently large to exclude cell volume adjustment.

2. Electronic Structure and Charge Distribution. Figure 1 shows the electron density of states (DOS) of Si, Ge, and Sn before and after the insertion of a neutral Li atom at the T-site. Upon the Li incorporation, the Fermi level shifts above the conduction band minimum, indicating that the charge transferred from Li partially fills the conduction band of the host. A grid-based Bader charge analysis³¹ predicts the amounts of electron transfer from the inserted Li to the Si, Ge, and Sn lattices to be 0.83e, 0.85e, and 0.87e, respectively; in the calculations, special care was taken to ensure convergence with respect to the grid size.

To evaluate the charge redistribution induced by the Li incorporation in the host matrix, the charge gain of the atoms adjacent to Li was calculated. As shown in Figure 2, the charge

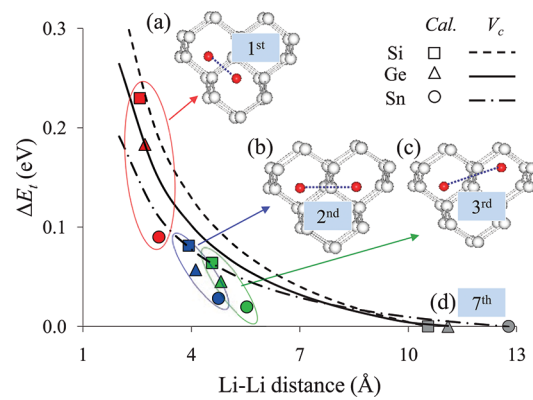


Figure 3. Variation in relative total energy (ΔE_t) as a function of Li–Li distance with respect to Li interstitials at a relatively large separation distance (~7th neighbor distance). The square, triangle, and circle markers represent calculated ΔE_t values (Cal.) in Si, Ge, and Sn, respectively, while the curve lines represent the estimated ΔE_t values using the Coulomb relation (V_C). Markers in red (blue and green) represent ΔE_t induced by Li interstitials separated by the 1st (2nd and 3rd) nearest T-site distance, as shown in inset (a) ((b) and (c)), where Li and host atoms are represented by red and white balls, respectively.

distributed to Si first NNs is the highest among the three host lattices, but with the increasing Si–Li distance, this amount also decreases most rapidly; from 0.24e (1st NNs) to 0.1e (2nd NNs) to 0.01e (3rd NNs) while there is no noticeable indication of charge gain beyond the third NNs. Relative to Si, the charge gain in Ge drops less rapidly from 0.13e (1st NNs) to 0.06e (2nd NNs) to 0.05e (3rd NNs). In the case of Sn, the charge redistribution range is extended farther to even the fourth NNs, from 0.15e (1st NNs), 0.04e (2nd NNs), and 0.03e (3rd NNs) to 0.02e (4th NNs). Overall, the excess charges are contributed by Li charge donation as well as the host atoms, from which electrons are redistributed toward the Li cation because of the electrostatic attraction. Therefore, the net charge gain can amount to a greater sum than that donated by Li alone. From Figure 2, we also see that the excess charges are more localized in Si and Ge, but farther spread in Sn. The largely localized charges within the first nearest neighbors are expected to effectively screen (or shield) the Li cation, and from our calculations, we anticipate this effect to be the most prominent in Si and least so in Sn.

3. Li–Li Interaction and Diffusion. As more Li atoms are inserted to the host lattice, it becomes important to understand the interaction between Li interstitials. Figure 3 shows the variations in the relative total energy (ΔE_t) with respect to state (d), at which Li atoms are separated at a relatively large distance (approximately seventh neighbor distance); one Li was at a T-site and the other was placed at the first (a), second (b), or third (c) neighboring T-site. The relative energies for (a), (b), and (c) are 0.23 (0.18, 0.09), 0.08 (0.06, 0.03), and 0.06 (0.05, 0.02) eV higher compared with that for (d) in Si (Ge, Sn). The curve lines in Figure 3 represent the idealized Coulomb electrostatic interaction between two point charges, $V_C = (q_1 q_2) / (4\pi \epsilon r)$, with respect to state (d); here, q is the Li cation charge ($q = 0.83e$, $0.85e$, and $0.87e$ for Li in Si, Ge, and Sn, respectively, according to the Bader charge analysis), r is the distance between two Li cations, and ϵ is the dielectric constant of the host lattice ($\epsilon = 1.05$, 1.42 , and 2.12×10^{-10} F/m for Si, Ge, and Sn, respectively).^{18,32}

Apparently, the energy increase with decreasing the Li–Li distance (r) is largely caused by the repulsive Coulomb interaction

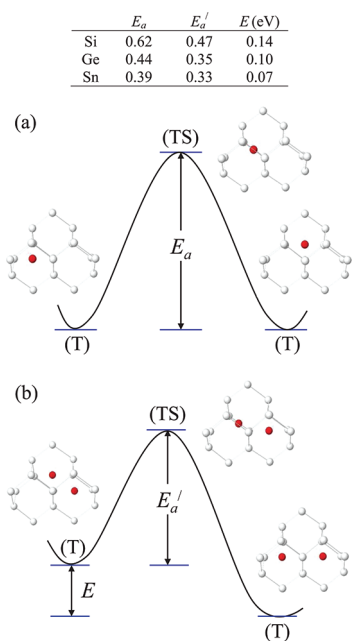


Figure 4. (a) Li diffusion pathway in Si, Ge, or Sn with the barrier values shown in the inset. Li jumps between two adjacent local minima (T; T-site) via a transition state (TS; H-site). (b) Li diffusion pathway under the influence of an adjacent Li atom. The black (red) and gray (white) balls represent Li and the host atoms, respectively.

between Li cations. The calculated cation repulsion (ΔE_r) is the strongest in Si and weakest in Sn; such a trend is also consistent with the idealized V_C prediction. Given that the repulsive potential is inversely proportional to the dielectric constant (ϵ) of the host lattice, Li cations are expected to repel each other most strongly in Si, which has the lowest dielectric constant among the three host materials. Additionally, we notice that the calculated ΔE_r are noticeably smaller than the V_C values. This is because the idealized Coulomb interaction assumes a perfect point charge and uniform charge distribution in the medium, and it does not address the charge redistribution and screening effects mentioned earlier. That is, the localized electrons surrounding Li may effectively shield the Li cations and lead to the reduction of the repulsive potential, as seen in our calculations.

Next, we evaluated the variations in the Li migration barrier as the host material changes. A Li interstitial may undergo migration by jumping between adjacent T-sites via a transition state (TS) hexagonal site (H-site), as shown in Figure 4a. The migration barrier (E_a) is calculated to be the largest in Si (0.62 eV), second largest in Ge (0.44 eV), and the smallest in Sn (0.39 eV). Among the three host materials, Sn has a more flexible lattice, which can expand easily to allow Li interstitials passing through, and its relatively larger atomic size also renders a more effective diffusion channel with a lower barrier. In the presence of an adjacent Li atom (Figure 4b), the diffusion barrier (E_a') is reduced to 0.47 eV in Si, 0.35 eV in Ge, and 0.33 eV in Sn owing to the repulsive interaction. The barrier reduction ($\Delta E = E_a - E_a'$) is proportional to the strength of the Li–Li electrostatic repulsion; that is, $\Delta E = 0.15$ eV (Si), 0.09 eV (Ge), and 0.06 eV (Sn). These results suggest that the migration barrier depends not only on the host lattice stiffness but also on the electrostatic interaction between diffusing species.³³ In addition, our study clearly demonstrates that Li interstitials favor to remain isolated and dispersed, rather than clustered, due to their cationic nature causing the repulsive interaction in the host materials.

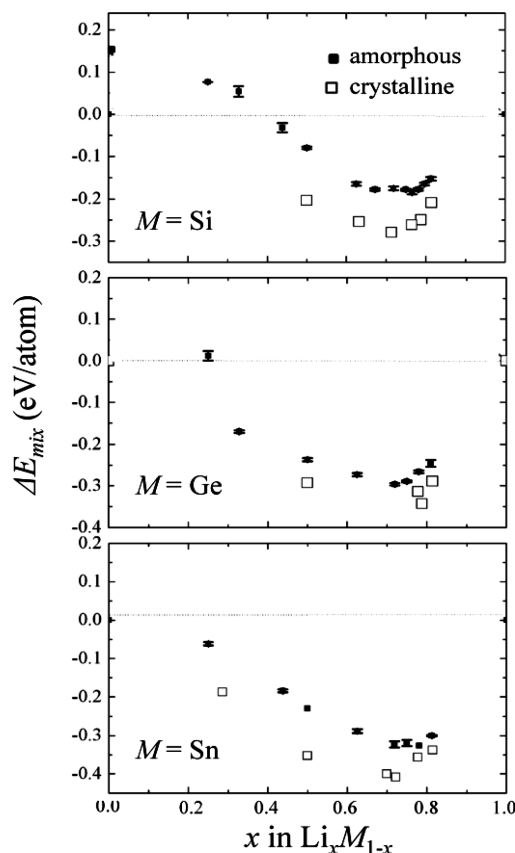


Figure 5. Variation in mixing enthalpy for amorphous and crystalline Li–M alloys as a function of Li content (x) in $\text{Li}_x\text{M}_{1-x}$.

B. Structure and Properties of Li–Si (Ge, Sn) Alloys.

1. Structure and Stability of Crystalline and Amorphous Phases. In the previous section, we discussed the behavior and properties of single Li interstitials in crystalline Si, Ge, and Sn. Here, we will look at the structure, energetics, and properties of crystalline and amorphous Li–M ($M = \text{Si}, \text{Ge}, \text{Sn}$) alloys as a function of Li content. Recent studies have provided evidence for the formation of various stable Li–M crystalline phases during high-temperature lithiation; the crystallographic parameters for the experimentally determined Li–M intermetallics are summarized in Table 3. However, room-temperature lithiation frequently leads to amorphous Li–M phases^{34–38} that may show different properties from their crystalline counterparts.

Figure 5 shows variations in the mixing enthalpy for amorphous and crystalline Li–M alloys as a function of the Li content, with respect to c-M and bcc-Li; for each amorphous alloy, the reported average value was obtained based on five independent 64-atom samples. The mixing enthalpy per atom (ΔE_{mix}) is given by

$$\Delta E_{\text{mix}} = E_{\text{Li}_x\text{M}_{1-x}} - xE_{\text{Li}} - (1-x)E_{\text{M}}$$

where $E_{\text{Li}_x\text{M}_{1-x}}$ is the total energy per atom of the alloy examined, x is the atomic fraction of Li, and E_{M} and E_{Li} are the total energies per atom of c-M and bcc-Li, respectively.

The mixing enthalpy results help evaluate the relative stabilities of the Li–M alloys. All three (Li–Si, Li–Ge, and Li–Sn) alloys display a general trend that the mixing enthalpy decreases with increasing Li content and falls to a valley plateau between 60 and 80 at. % Li. Note that the mixing enthalpies for Li–Si and Li–Ge alloys at low Li contents are positive in value with respect

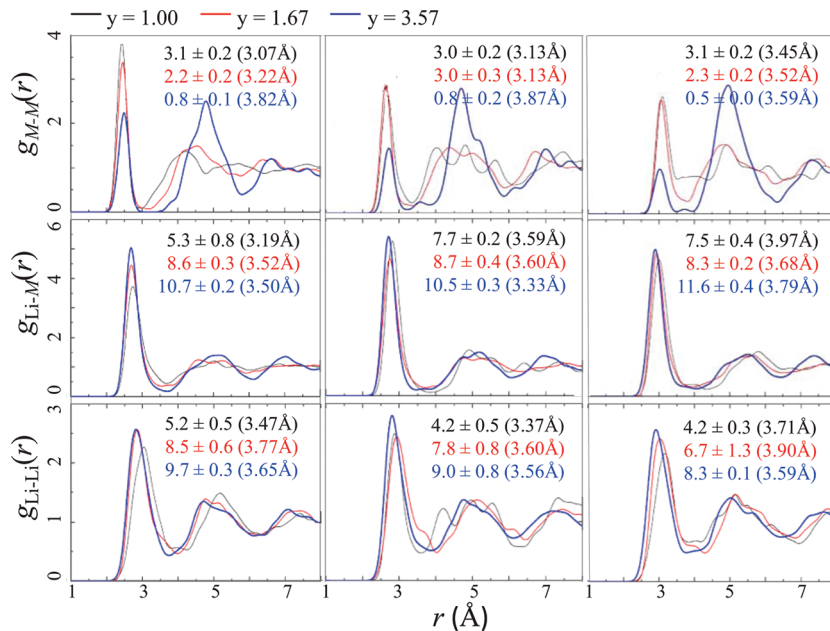


Figure 6. Pair distribution functions $g(r)$ for Li_yM alloys ($\text{M} = \text{Si}, \text{Ge}, \text{Sn}; y = 1, 1.67, \text{and } 3.57$). For each plot, the average coordination number with the corresponding cut-off radius in parentheses is shown in the upper right-hand corner.

to their crystalline host lattices, but as the Li content increases, those values drop and change from positive to negative at around 40 (25) at. % Li for $\text{Li}-\text{Si}$ ($\text{Li}-\text{Ge}$) alloys. The positive value of the mixing enthalpy at low Li contents may indicate the presence of an initial barrier for Li incorporation into the crystalline host matrixes. Contrarily, the negative mixing enthalpy suggests favorable alloy formation.

According to the results, amorphous $\text{Li}-\text{Sn}$ alloys with 60–80 at. % Li are the most favorable with an energy gain of $\Delta E_{\text{mix}} = 0.30\text{--}0.33 \text{ eV/atom}$ with respect to c-M and bcc-Li, followed by $\text{Li}-\text{Ge}$ alloys with $\Delta E_{\text{mix}} = 0.25\text{--}0.29 \text{ eV/atom}$, and $\text{Li}-\text{Si}$ alloys are the least favorable with $\Delta E_{\text{mix}} = 0.16\text{--}0.18 \text{ eV/atom}$. For the crystalline phases, distinct mixing enthalpy minima are found at 70 at. % Li for $\text{Li}-\text{Si}$ and $\text{Li}-\text{Sn}$, whereas 80 at. % Li for $\text{Li}-\text{Ge}$ alloys. On average, the amorphous phases are about 0.1 eV/atom less favorable than their crystalline counterparts, suggesting the possibility of recrystallization at elevated temperatures, as evidenced by earlier experiments.⁴⁶

For each $\text{Li}-\text{M}$ alloy, three compositions were selected to analyze the structural variations as the Li content increases from $y = 1$ to 1.67 to 3.57 . The amorphous structures are characterized using the pair distribution function (PDF, $g(r)$), which is defined as⁴⁷

$$g(r) = \frac{V}{N} \frac{n(r)}{4\pi r^2 \Delta r}$$

where $n(r)$ represents particles in a shell within the region $r \pm \Delta r/2$, Δr is the shell thickness, and N denotes the number of particles in the model volume V .

For the PDFs presented in Figure 6, five independent 64-atom samples were used for each composition to obtain good statistics. In contrast to the typical sharp lines found in crystalline materials, the PDF peaks of Li_yM alloys are smoother and more broadened while no long-range order can be identified, indicating an amorphous nature. Looking at the first peak intensities, we find that the $\text{Li}-\text{M}$ and $\text{Li}-\text{Li}$ peaks become stronger while the $\text{M}-\text{M}$ peaks dwindle as the Li content increases. We also notice that,

with increasing Li content, the $\text{M}-\text{M}$ peak positions shift to larger pair distances, whereas the opposite trends are found for the $\text{Li}-\text{Li}$ peaks. The increased $\text{M}-\text{M}$ pair distance is indicative of the weakened $\text{M}-\text{M}$ interaction; note that transferred charge from Li fills up the antibonding states of the host elements and thereby weakens the $\text{M}-\text{M}$ bonds even at low Li contents, as discussed in ref 30. In Figure 6, upper right-hand corner, the average coordination numbers (CNs) were calculated based on integration of the first peak of $g(r)$ with the corresponding cut-off radius (first peak minimum) in parentheses. As the Li content (y) increases from 1 to 3.57, the $\text{CN}_{\text{M}-\text{M}}$ decreases while the $\text{CN}_{\text{Li}-\text{M}}$ and $\text{CN}_{\text{Li}-\text{Li}}$ increase ($\text{CN}_{\text{Si}-\text{Si}}$, 3.1 to 0.5; $\text{CN}_{\text{Ge}-\text{Ge}}$, 3.0 to 0.8; $\text{CN}_{\text{Sn}-\text{Sn}}$, 3.1 to 0.5). The decrease in $\text{CN}_{\text{M}-\text{M}}$ indicates that the host lattice gradually loses its connectivity, whereas the $\text{Li}-\text{M}$ alloys become more densely packed with the increasing Li content, as is evident by the increasing $\text{CN}_{\text{Li}-\text{M}}$ and $\text{CN}_{\text{Li}-\text{Li}}$.

On the basis of the model structures, the variations in volume (V) as a function of Li content (y) were calculated (Figure 7); the volume of each alloy is normalized with respect to that of the pure host matrix. For both amorphous and crystalline phases, V increases nearly linearly with y , and the crystalline phases are slightly denser than the amorphous counterparts as expected. At highly lithiated states, the predicted volume expansions for amorphous (crystalline) phases in the order from small to large is $\text{Li}_{4.33}\text{Sn}$, 305 (259)%; $\text{Li}_{4.33}\text{Ge}$, 382 (353)%; and $\text{Li}_{4.33}\text{Si}$, 434 (399)%, which are in good agreement with the previous experimental measurements of $\text{Li}_{4.4}\text{Sn}$, 260%;⁵ $\text{Li}_{4.4}\text{Ge}$, 370%;⁴ and $\text{Li}_{4.4}\text{Si}$, 400%.³ $\text{Li}-\text{Sn}$ alloys have the lowest volume expansion because Sn can accommodate Li more easily due to its flexible matrix and larger interstitial space (recall the discussion in section 3.A.1).

2. Electronic and Mechanical Properties. We calculated the charge states of crystalline $\text{Li}-\text{M}$ alloys with selected Li contents using the Bader method³¹ (Table 4). These crystalline phases are generally understood to be Zintl-like phases⁴⁸ with the consideration that only a partial charge is transferred from Li (Si, Ge, or Sn is not electronegative enough to completely strip off the outer

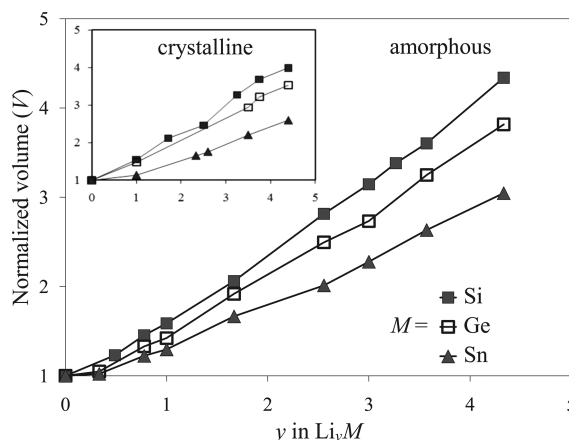


Figure 7. Variation in volume as a function of Li content (y). The volume of each alloy is normalized with respect to its pure phase. For amorphous phases, five independent 64-atom samples were used for each composition to obtain good statistics.

Table 4. Calculated Charge States of Li and M in Crystalline Li–M Alloys Using Grid-Based Bader Charge Analysis

element/phase	LiSi	LiGe	LiSn	Li ₁₅ Si ₄	Li ₁₅ Ge ₄	Li ₇ Sn ₂
Si, Ge, Sn	-0.84	-0.84	-0.85	-3.08	-3.08 ^a	-3.30/-2.46 ^b
Li	+0.84	+0.84	+0.85	+0.82	+0.82	+0.82

^a In Li₁₅Si₄ and Li₁₅Ge₄, each atom (Si or Ge) has 12 Li neighbors. ^b In Li₇Sn₂, two different clusters are present: Sn with 14 Li neighbors, and Sn with 12 Li plus 1 Sn neighbors.

shell (2s) electron from Li). If every Li atom donates its 2s electron to M, the charge transfer in Li_yM is represented as $(\text{Li}^+)_y \text{M}^{y-}$, and in the case of $y < 4$, $(4 - y)$ M–M bonds per M atom are formed to satisfy the $(8 - N)$ octet rule. LiSi is isostructural with LiGe, and both are Zintl phases ($y = 1$) with Si and Ge having 3-fold coordination ($4 - 1 = 3$) and a -0.84 charge state ($0.84e$ donated by Li). Contrarily, LiSn does not share the same structure with LiSi or LiGe; it is intermediate between the perfect ionic phase and the Zintl polyanionic compound, and Sn (in LiSn) is four-coordinated with a -0.85 charge state. Li₁₅Si₄ and Li₁₅Ge₄ are the first Zintl phases where all the Si and Ge atoms are isolated and surrounded by Li atoms ($y = 3.75$; number of Si–Si and Ge–Ge bonds = 0.25); in these cases, the charge states of Si and Ge are both -3.08 (each Li donates $0.82e$). In the Li₇Sn₂ Zintl phase, two different Sn clusters are present: (a) Sn surrounded by 14 Li neighbors and (b) Sn surrounded by 12 Li plus 1 Sn neighbors. Because of the variation in cluster configuration, the former has a -3.30 charge state (each Li donates $0.82e$) and the latter has a -2.46 charge state (each Li donates $0.82e$). We see that the Li charge state remains nearly unchanged ($+0.82 \sim +0.84$), whereas the charge state of M varies with the local Li–M and M–M coordinations. With the increasing net charge transfer in the higher lithiated phases, the filling of the host element antibonding p states leads to significant s–p splitting (ref 49), weakened M–M bonds, and, consequently, the fragmentation/disintegration of the host lattice.

As the M–M covalent bonds are replaced with more ionic Li–M bonds in Li–M alloys of higher Li contents, we expect to see a decrease in the modulus since Li–M and Li–Li bonds are weaker compared to M–M covalent bonds. To evaluate the effect of Li content on the mechanical properties, we calculated

Table 5. Parameterizations of the Strains Applied to Calculate Elastic Constants of Cubic LiGe, Li₁₅Si₄, and Li₁₅Ge₄, and Tetragonal LiSi, Li₂Sn₅, and Li₇Sn₂

strain	parameters (unlisted $e_{ij} = 0$)	$\Delta E/V$
cubic phase		
1	$e_1 = e_2 = \gamma, e_3 = (1 + \gamma)^{-2} - 1$	$3(C_{11} - C_{12})\gamma^2$
2	$e_1 = e_2 = e_3 = \gamma$	$3/2(C_{11} + 2C_{12})\gamma^2$
3	$e_6 = \gamma, e_3 = \gamma^2(4 - \gamma^2)^{-1}$	$1/2C_{44}\gamma^2$
tetragonal phase		
1	$e_1 = 2\gamma, e_2 = e_3 = -\gamma$	$1/2(5C_{11} - 4C_{12} - 2C_{13} + C_{33})\gamma^2$
2	$e_1 = e_2 = -\gamma, e_3 = 2\gamma$	$(C_{11} + C_{12} - 4C_{13} + 2C_{33})\gamma^2$
3	$e_1 = e_2 = \gamma, e_3 = -2\gamma, e_6 = 2\gamma$	$(C_{11} + C_{12} - 4C_{13} + 2C_{33} + 2C_{66})\gamma^2$
4	$e_1 = \gamma$	$1/2C_{11}\gamma^2$
5	$e_3 = \gamma$	$1/2C_{33}\gamma^2$
6	$e_4 = 2\gamma$	$2C_{44}\gamma^2$

the elastic constants of several crystalline phases of selected Li contents. Elastic constants, C_{ij} , can be obtained by computing the energies of deformed unit cells; the deformation strain tensor, \mathbf{e} , with six independent components is represented as

$$\mathbf{e} = \begin{pmatrix} e_1 & e_6/2 & e_5/2 \\ e_6/2 & e_2 & e_4/2 \\ e_5/2 & e_4/2 & e_3 \end{pmatrix}$$

For cubic phases (LiGe, Li₁₅Si₄, and Li₁₅Ge₄), orthorhombic, isotropic, and monoclinic distortions were applied to obtain three independent elastic constants, C_{11} , C_{12} , and C_{44} (expressed using Voigt notations). For tetragonal phases (LiSi, Li₂Sn₅, and Li₇Sn₂), six independent deformation modes were applied to calculate C_{11} , C_{12} , C_{13} , C_{33} , C_{44} and C_{66} . Self-consistent relaxation is allowed in all strained unit cells, and the total energy change with respect to the strain tensor gives^{50,51}

$$E(\mathbf{e}) = E_0 - P(V)\Delta V + \frac{V}{2} \sum_{ij} C_{ij} e_i e_j + O[\mathbf{e}^3]$$

where E_0 and $E(\mathbf{e})$ are the internal energies of the initial and strained lattices, respectively; V is the volume of the unstrained lattice; $P(V)$ is the pressure of the undistorted lattice at volume V ; ΔV is the change in the volume of the lattice due to the strain; \mathbf{e} is the strain tensor; and $O[\mathbf{e}^3]$ indicates the neglected terms in the polynomial expansion.

Table 5 summarizes the parameterizations^{50,51} of the strains applied with the strain value, γ ranging from -0.01 to 0.01 in 0.003 increments. The calculation of the elastic constant requires a high degree of precision because the energy variation involved is very small; hence, the geometry optimization was performed at a higher cut-off energy of 500 eV and a tighter force tolerance of 0.001 eV. Once C_{ij} values are known, mechanical quantities, such as Poisson's ratio and Young's, bulk, and shear moduli, can be calculated. Here, we only report the bulk modulus B , of particular interest for the purpose of our study, that is given by $B = 1/9(C_{11} + C_{22} + C_{33} + 2C_{12} + 2C_{13} + 2C_{23})$. The computed elastic constants and bulk moduli are summarized in Table 6. The calculated $B(\text{c-SiLi}) = 64.78$ GPa and $B(\text{c-Si}_{15}\text{Li}_4) = 32.36$ GPa are in good agreement with the previously reported calculated

Table 6. Calculated Elastic Constants and Bulk Moduli for Crystalline Li–Si, Li–Ge, and Li–Sn Alloys; Values Calculated by Others Are in Parentheses⁵²

phases	C_{11}	C_{33}	C_{12}	C_{13}	C_{44}	C_{66}	B (GPa)
LiSi	109.0 (101.16)	71.7 (74.506)	24.9 (20.645)	39.0 (37.343)	54.6 (55.435)	37.9 (36.000)	55.1
LiGe	72.1	43.5	27.2	30.5	23.8	13.9	40.4
Li ₂ Sn ₅	96.4	136.4	111.9	28.8	112.8	9.3	74.2
Li ₁₅ Si ₄	55.9 (46.644)		20.6 (21.907)		33.9 (28.019)		32.4
Li ₁₅ Ge ₄	43.1		19.8		31.0		27.6
Li ₇ Si ₂	61.5	88.6	22.1	3.3	63.3	40.9	29.9

values of 53.0 and 30.0 GPa, respectively.⁵² For a given Li content, Li–Ge and Li–Sn alloys tend to be softer than the Li–Si alloy. Clearly, the bulk modulus decreases with increasing Li content, leading to significant elastic softening, which is consistent with our expectation from the analysis of the Li–M bonding nature.

4. CONCLUSION

On the basis of DFT-GGA calculations (LDA was also used in some selected cases for comparison), comparative analyses were carried out to study the behavior and nature of Li incorporation in different host materials, M (M = Si, Ge, and Sn). Crystalline and amorphous Li–M alloys were then examined in terms of their energetics, structural evolution, and electronic and mechanical properties. The lattice disturbance associated with Li insertion is significant in Si, but minimal in Sn, due to its relatively larger interstitial space and softer matrix, and thus Li incorporation is found to be the most (least) favorable in Sn (Si). The electronic structure analysis highlights the charge transfer from Li to M, and using the grid-based Bader analysis, the amounts of electron donation were estimated to be 0.83e (Si), 0.85e (Ge), and 0.87e (Sn). These transferred charges can fill the host element antibonding states, leading to the weakened M–M bonds. Also associated with the cationic nature of Li, electrons in the host are redistributed toward Li; as the excess charges are more localized (farther spread) in Si (Sn), the charge screening/shielding effect is the strongest (weakest) in Si (Sn). Li atoms inside the host materials can easily undergo migration by overcoming small-to-moderate barriers of 0.39 eV (Sn), 0.44 eV (Ge), and 0.62 eV (Si), and owing to the Li⁺–Li⁺ repulsive interaction, which is the strongest in Si and the weakest in Sn, Li interstitials have a strong tendency to remain isolated and well dispersed in the hosts. According to our mixing enthalpy calculations, alloying between Li and M is energetically favorable with the most stable compositions occurring between 60 and 80 at. % Li. Li–Sn alloys are more stable than Li–Ge and Li–Si alloys, and when fully lithiated, the volume expansion for the amorphous (crystalline) alloys are Si, 434%; Ge, 382%; and Sn, 305% (Si, 399%; Ge, 353%; and Sn, 259%), respectively. From the structure and grid-based Bader charge analyses, we see that the coordination and bonding of M atoms in crystalline Li–M phases generally reflect what is to be expected by Zintl rules. Furthermore, with the increase in Li content, the host network disintegrates as the covalent M–M bonds are replaced by the weaker ionic Li–M and metallic Li–Li bonds, leading to the softening of Li–M alloys at highly lithiated states, as demonstrated by our mechanical property calculations. These fundamental findings add to the understanding of the nature of Li incorporation and alloying with Si, Ge, and Sn; moreover, the present work may provide a framework for the comparative study of various lithiated alloys.

■ AUTHOR INFORMATION

Corresponding Author

*E-mail: gshwang@che.utexas.edu.

■ REFERENCES

- Park, C. M.; Kim, J. H.; Kim, H.; Sohn, H. J. *Chem. Soc. Rev.* **2010**, 39, 3115.
- Zhang, W. J. *J. Power Sources* **2011**, 196, 13.
- Kasavajjula, U.; Wang, C.; Appleby, A. J. *J. Power Sources* **2007**, 163, 1003.
- Chen, C. K.; Zhang, X. F.; Cui, Y. *Nano Lett.* **2008**, 8, 307.
- Winter, M.; Besenhard, J. O. *Electrochim. Acta* **1999**, 45, 31.
- Netz, A.; Huggins, R. A.; Weppner, W. *J. Power Sources* **2003**, 95, 119.
- Bourderau, S.; Brousse, T.; Schleich, D. M. *J. Power Sources* **1999**, 233, 81.
- Hatchard, T. D.; Dahn, J. R. *J. Electrochem. Soc.* **2004**, 151, A838.
- Gao, B.; Sinha, S.; Fleming, L.; Zhou, O. *Adv. Mater.* **2001**, 13, 816.
- Graetz, J.; Ahn, C. C.; Yazami, R.; Fultz, B. *Electrochem. Solid-State Lett.* **2003**, 6, A194.
- Chan, C. K.; Peng, H.; Liu, G.; McIlwraith, K.; Zhang, X. F.; Huggins, R. A.; Cui, Y. *Nat. Nanotechnol.* **2008**, 3, 31.
- Beaulieu, L. Y.; Hewitt, K. C.; Turner, R. L.; Bonakdarpour, A.; Abdo, A. A.; Christensen, L.; Eberman, K. W.; Krause, L. J.; Dahn, J. R. *J. Electrochem. Soc.* **2003**, 150, A149.
- Mao, O.; Turner, R. L.; Courtney, I. A.; Fredericksen, B. D.; Buckett, M. I.; Krause, L. J.; Dahn, J. R. *Electrochem. Solid-State Lett.* **1999**, 2, 3.
- Fleischauer, M. D.; Topple, J. M.; Dahn, J. R. *Electrochem. Solid-State Lett.* **2005**, 8, A137.
- Beaulieu, L. Y.; Hatchard, T. D.; Bonakdarpour, A.; Fleischauer, M. D.; Dahn, J. R. *J. Electrochem. Soc.* **2003**, 150, A1457.
- (a) Nazri, G. A.; Pistoia, G. *Lithium Batteries Science and Technology*; Kluwer Academic Plenum: Boston, 2004. (b) Anani, A.; Crouch-Baker, S.; Huggins, R. A. *J. Electrochem. Soc.* **1987**, 134, 3098.
- Graetz, J.; Ahn, C. C.; Yazami, R.; Fultz, B. *J. Electrochem. Soc.* **2004**, 151, A698.
- Lide, D. R., Ed. *CRC Handbook of Chemistry and Physics*, 80th ed.; CRC Press: Boca Raton, FL, 1999; p 14.
- Blochl, P. E. *Phys. Rev. B* **1994**, 50, 17953.
- Kresse, G.; Hafner, J. *Phys. Rev. B* **1993**, 47, 558.
- Kresse, G.; Furthmüller, J. *Comput. Mater. Sci.* **1996**, 6, 15.
- Kresse, G.; Furthmüller, J. *Phys. Rev. B* **1996**, 54, 11169.
- (a) Monkhorst, H. J.; Pack, J. D. *Phys. Rev. B* **1976**, 13, 5188. (b) Rahman, A. *Phys. Rev.* **1964**, 146, A405.
- Henkelman, G.; Blas, P. U.; Hannes, J. *J. Chem. Phys.* **2000**, 113, 9901.
- Lee, S.-H.; Hwang, G. S. *J. Chem. Phys.* **2007**, 127, 224710.
- Murnaghan, F. D. *Proc. Natl. Acad. Sci. U.S.A.* **1994**, 30, 244.
- Wang, S. Q.; Ye, H. Q. *J. Phys.: Condens. Matter* **2003**, 15, L197.
- Gersten, J. I.; Smith, F. W. *The Physics and Chemistry of Materials*; John Wiley & Sons, Inc.: New York, 2001; p 23.

- (29) Aguado, A. *Phys. Rev. B* **2003**, *67*, 212104.
- (30) Kim, H. W.; Kweon, K. E.; Chou, C. Y.; Ekerdt, J. G.; Hwang, G. S. *J. Phys. Chem. C* **2010**, *114*, 17942.
- (31) Henkelman, G.; Arnaldsson, A.; Jónsson, H. *Comput. Mater. Sci.* **2006**, *36*, 254.
- (32) Sze, S. M. *Physics of Semiconductor Devices*; John Wiley and Sons, Inc.: New York, 1981.
- (33) Sharma, N. D.; Kasir, F. A. *J. Phys. Soc. Jpn.* **1979**, *47*, 1025.
- (34) Maranchi, J. P.; Hepp, A. F.; Kumta, P. N. *Electrochem. Solid-State Lett.* **2003**, *6*, A198.
- (35) Limthongkul, P.; Jang, Y.-I.; Dudney, N.; Chiang, Y.-M. *Acta Mater.* **2003**, *51*, 1103.
- (36) Limthongkul, P.; Jang, Y.-I.; Dudney, N.; Chiang, Y.-M. *J. Power Sources* **2003**, *604*, 119.
- (37) Huang, H.; Li, X. L.; Chen, G.; Zhou, Z.; Zhang, D. Y.; Mo, Y. J.; Pei, N. *Solid State Ionics* **2000**, *135*, 181.
- (38) Seo, M. H.; Park, M.; Lee, K. T.; Kim, K.; Kim, J.; Cho, J. *Energy Environ. Sci.* **2011**, *4*, 425.
- (39) Stearns, L. A.; Gryko, J.; Diefenbacher, J.; Ramachandran, G. K.; McMillan, P. F. *J. Solid State Chem.* **2003**, *173*, 251.
- (40) Böhm, M. C.; Ramirez, R.; Nesper, R.; Schnerring, H. G. *Phys. Rev. B* **1984**, *30*, 4870.
- (41) Okamoto, H. *Bull. Alloy Phase Diagrams* **1990**, *11*, 306 and references cited therein.
- (42) Kubota, Y.; Escao, M. C. S.; Nakanishi, H.; Kasai, H. *J. Appl. Phys.* **2007**, *102*, 053704.
- (43) Sangster, J.; Pelton, A. D. *J. Phase Equilib.* **1997**, *18*, 118 and references cited therein.
- (44) Hansen, D. A.; Chang, L. J. *Acta Crystallogr., Sect. B* **1969**, *25*, 2392.
- (45) Sangster, J.; Bale, C. W. *J. Phase Equilib.* **1998**, *19*, 70 and references cited therein.
- (46) Sharma, R. A.; Seefurth, R. N. *J. Electrochem. Soc.* **1976**, *123*, 1763.
- (47) Allen, M.; Tildesley, D. *Computer Simulation of Liquids*; Oxford University Press: New York, 1987; p 54.
- (48) Kauzlarich, S. M. *Chemistry, Structure, and Bonding of Zintl Phases and Ions*; Wiley-VCH Publishers: New York, 1996.
- (49) Kim, H.; Chou, C. Y.; Ekerdt, J. G.; Hwang, G. S. *J. Phys. Chem. C* **2011**, *115*, 2514.
- (50) Mehl, M. J.; Klein, R. M.; Papaconstantopoulos, D. A. In *Intermetallic Compounds: Principles and Practice*; Westbrook, J. H., Fleischer, R. L., Eds.; John Wiley and Sons: London, 1995; Vol. I, Chapter 9, p 195.
- (51) Beckstein, O.; Klepeis, J. E.; Hart, G. L. W.; Pankratov, O. *Phys. Rev. B: Condens. Matter* **2001**, *63*, 1341121.
- (52) Shenoy, V. B.; Johari, P.; Qi, Y. *J. Power Sources* **2010**, *195*, 6825.